공학석사 학위논문

Structural Safety Assessment of Cargo Containment System in LNG Carrier under Iceberg Collision

빙산 충돌에 대한 LNG선 화물창 단열시스템의 안전성 평가

지도교수 이 상 갑

20010년 2월

한국해양대학교 대학원

해양시스템공학과

이 재 석

본 논문을 이재석의 공학석사 학위논문으로 인준함.

위원장 : 공학박사 손 경 호 (인)

위 원 : 공학박사 박 석 주 (인)

위 원 : 공학박사 이 상 갑 (인)

2010년 2월

한국해양대학교 대학원

해양시스템공학과 이 재 석

목 차

List of Tables

List of Figures

Structural Safety Assessment of Cargo Containment System in LNG Carrier under Iceberg Collision

Lee, Jae-seok

Division of Ocean Systems Engineering

Graduate School, Korea Maritime University

Abstract

At the time of exploitation of the giant natural gas fields in the Western Arctic regions of Russia, the development of Arctic LNG shipping has been precipitated. There have been demands for the security of design technique of Arctic LNG carrier, especially for the structural safety assessment of the Arctic LNG CCS under the impact of collision with iceberg. To develop iceberg modeling technique and to examine the characteristics of iceberg crushing strength for the more accurate and realistic full scale iceberg-membrane type LNG carrier bow shoulder collision simulations with consideration of surrounding sea water using FSI (Fluid-Structure Interaction) analysis technique, uniaxial compressive ice test specimen simulations in brittle and ductile failure modes were executed and diverse iceberg materials were investigated using LS-DYNA code, such as its failure strain, Young's modulus, failure stress, failure tensile stress and mesh size. Local zooming analysis of MARK III membrane type LNG CCS according to iceberg sizes and failure strains were performed for the development of its structural safety assessment technique.

빙산 충돌에 대한 LNG선 화물창 단열시스템의 안전성 평가

이 재석

한국해양대학교 대학원

조선해양시스템공학과

요 약

러시아 서부 극지지역에서의 대규모 천연가스(Liquified Natural Gas) 개발과 함께 극지운항 LNG선의 수주가 증가함에 따른 설계 기술력의 확보가 요구되고 있고, 특히 빙산(iceberg)과의 충돌에 대한 LNG선 화물창 단열시스템(CCS; Cargo Containment System) 구조의 안전성 검증이 매우 중요하다. 보다 정확하고 현실적인 빙산 모델링 기술의 개발과 빙산 분쇄강도(crushing strength)의 특성을 구현하기 위해서 LS-DYNA 코드의 유체-구조 연성(FSI; Fluid-Structure Interaction) 해석기법을 사용하여 주변유체를 고려한 LNG선과의 선수 어깨부위(bow shoulder) 충돌 시뮬레이션을 수행하였다. 또한 취성 및 연성 파손모드에서의 빙(ice) 시험용 시편의 일축압축 시뮬레이션을 수행하였고, 파단변형률(failure strain), 탄성계수(Young‘s modulus), 파단응력(failure stress), 파단 인장응력(failure tensile stress) 및 유한요소 크기(mesh size) 등과 같은 다양한 빙산의 물성치에 대한 패러미터 연구를 수행하였다. 구조 안전성 평가기법의 개발을 위하여 빙산의 크기와 파단변형률을 고려한 MARK Ⅲ 멤브레인형 LNG CCS의 Local Zooming Analysis의 기법을 개발하여 적용하였다.

1. Introduction

The size of LNG (Liquefied Natural Gas) carriers has been increased with the worldwide increasing demands of LNG and the necessities of economic transportation, which would cause their cargo tank size and configuration. Since there is no internal supporting structure, such as partial bulkhead, due to cryogenic liquid properties in the cargo tanks of LNG carriers, sloshing impact loading could be one of the most important factors for the structural safety of LNG Cargo Containment System (CCS). At the time of exploitation of the giant natural gas fields in the Western Arctic regions of Russia, the development of Arctic LNG shipping has been precipitated. There have been demands for the security of design technique of Arctic LNG carrier, especially for the structural safety assessment the Arctic LNG CCS under the impact of collision with iceberg.

The most important structural safety criterion of membrane type LNG carrier might be the leakage of LNG from CCS under the LNG sloshing impact loading inside the cargo tank holds, and under level ice compressive contact or iceberg collision impact loadings outside the cargo tank. For the reasonable and reliable safety assessment of CCS, its criteria should be set up from the viewpoints of large deformation and strength of CCS under the quasi-static loading condition, and of deformation and strength of its components and its attachment to the inner hull under impact loading ones.

The structural safety assessment of LNGC CCS under the iceberg-ship collision will depend on the connection methods of CCS to inner hull. While NO96 membrane type CCS in Fig. 1.1 is attached to inner hull by the coupler, MARK III membrane type CCS in Fig. 1.2, by the mastic. Since the former is not directly attached to the inner hull and its deformation is absorbed by the coupler, it is known that it is designed to withstand the inner hull deformation with flexibility. The criterion of safety assessment of NO96 membrane type

CCS is the magnitude of deformation to sustain without transformation of force from the coupler to CCS.

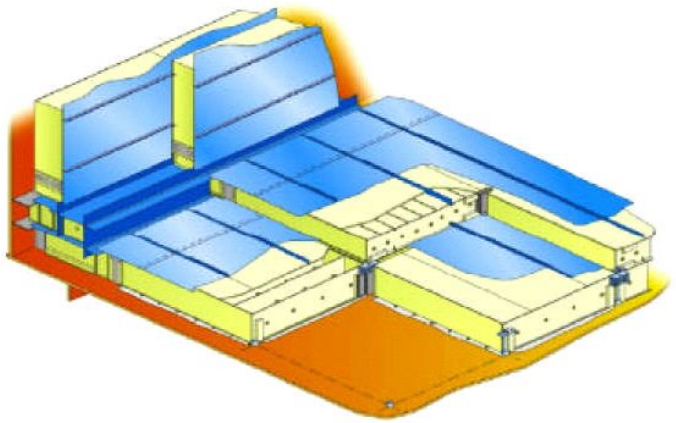

Fig. 1.1 NO96 Cargo Containment System

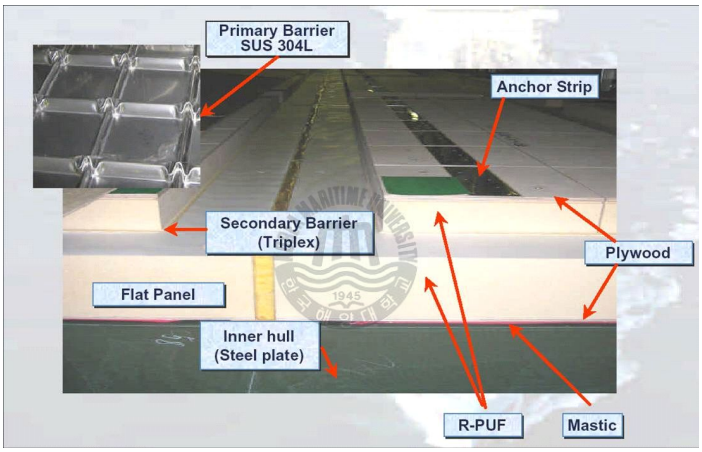

Fig. 1.2 MARK III Cargo Containment System

Figure 1.3 shows the allowable deformation for the safety status of NO96 membrane type CCS, where 4.6 mm per unit m is allowed as Operational limit, and 40.0mm per unit m, as survival limit (Lee et al. 2007, Han et al. 2007). However, the safety of coupler under shock vibration should be also considered. In the MARK III membrane type CCS, more weight seems to be placed on the safety of the inner hull and mastic of CCS by the shock vibration under iceberg-ship collision.

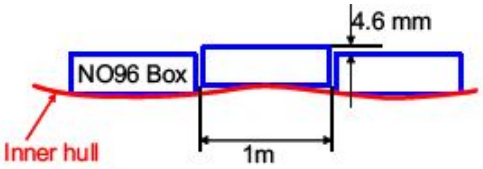

Fig. 1.3 Operational limit (Lee et al. 2007)

For the reasonable and reliable safety assessment of LNG CCS, it is important to predict the contact or impact loadings to CCS under LNG sloshing inside the cargo tank holds or under level ice compressive contact or iceberg collision outside the cargo tank in addition to the establishment of criterion for the deformation and strength of its components and attachment to the inner hull. More accurate and realistic iceberg-ship collision analysis technique with consideration of surrounding sea water was developed using LS-DYNA code (LSTC 2007), and diverse scenarios of full scale iceberg-ship collision simulations were carried out for the examination of their effects on the collision responses, such as analysis techniques FSI and MCOL, elastic and ice type iceberg materials, iceberg shape, size, attack angle, LNG carrier speed and inner fluid (Lee et al. 2009).

In addition to the analysis technique, it could be also very important to figure out the characteristics of iceberg crushing strength and their effects on the collision responses for the more accurate and realistic responses in the inner hull from full scale iceberg-ship collision simulation. For the examination of its material characteristics, such as brittle and ductile failure modes, uniaxial compressive ice test specimen simulation would be helpful with its test results. Several material properties of iceberg, such as failure strain, failure strength, Young's modulus and failure tensile strength, could have an influence on its crushing strength, which might be necessary to be simulated for the examination of their effects on the collision responses.

The objectivity of accurate and realistic responses in the inner hull from full scale iceberg-ship collision simulation would be the reasonable structural safety assessment of membrane type CCS. However, it is very difficult to carry out

the full scale iceberg-ship collision simulation together with very small fine mesh CCS model considering surrounding sea water, because of the characteristics of explicit hydrocode LS-DYNA, etc. It could be very useful to adopt the local zooming analysis technique for the structural safety assessment of CCS.

The objective of this study is to develop a more accurate and realistic iceberg-ship collision analysis technique FSI with iceberg modeling technique using LS-DYNA code and structural safety assessment technique of LNG CCS using zooming analysis. Uniaxial compressive ice test specimen simulations in brittle and ductile failure modes were also executed for the estimation of the characteristics of iceberg crushing strength. As mentioned above, diverse scenarios of full scale iceberg-ship collision simulations were carried out for the examination of their effects on the collision responses, such as failure strain, failure strength, Young's modulus, failure tensile strength and mesh size. Using local zooming analysis, structural safety assessments of MARK III membrane type CCS according to iceberg sizes and failure strains were performed for the development of their techniques.

2. Ice Characteristics

Ice has typical characteristics with diverse mechanical properties, such as density, strength and Young's modulus, etc, depending on temperature, salinity, porosity, grain and strain rate. Ice also shows peculiar characteristics under tension and compression conditions, differently from the other materials, whose properties give a very important affects on the determination of ice loads. While the compressive strength is strain rate sensitive, the tensile strength is strain rate insensitive. Figure 2.1 shows schematic stress-strain curves, where curves I, II, and III denote low-, intermediate-, and high-strain rates, and the arrows indicate either ductile (horizontal) or brittle (vertical) behavior. Tensile stress-strain curves exhibit ductile behavior at low strain rates, but brittle behavior at intermediate and high strain rates. Compressive stress-strain curves show ductile behavior at low and intermediate strain rates, but brittle behavior at high strain rates (Carney 2006, Schulson 1999, 2001).

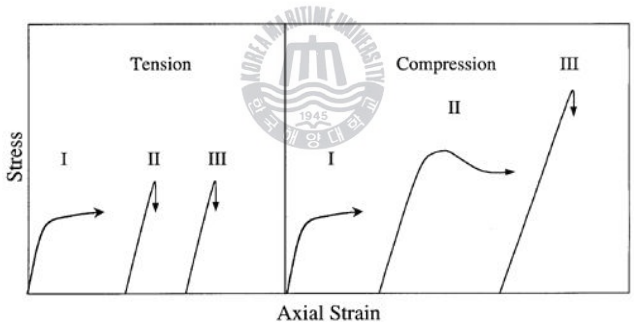

Fig. 2.1 Schematic stress-strain curves

Figure 2.2 shows measurements of tensile and compressive strength obtained from fresh-water ice about 1 mm in grain size loaded uniaxially at temperatures around -10°C. It can be found that ice exhibits a variety of behaviors, ranging from ductile to brittle, as a function of strain rate in compression, as shown in Fig. 2.3. The ductile to brittle transition occurs at a

strain rate on the order of 10^{-3} s^{-1}, under uniaxial compression, at temperatures on the order of -10°C, as shown in Fig. 2.2, with a dramatic increase for polycrystalline ice in the compressive failure stress from 0.5 MPa at a strain rate of 10^{-8} s^{-1} to 10.0 MPa at a strain rate of 10^{-3} s^{-1}, then a decline to 6.0 MPa at 10^{-1} s^{-1} (Schulson 2001). It was also reported that the compressive failure stress was independent of strain rate in the range 10^{-2} s^{-1} to 10^{-1} s^{-1} and rate in the range 100 s^{-1} to 10^{2} s^{-1} (Carney 2006). It can be also found that the tensile strength is strain rate insensitive compared to the compressive strength.

Figure 2.4 exhibits an another compressive uniaxial failure strength of S-2 ice according to strain rate, which proposed an effectively empirical universal curve for indentation of S-2 ice (solid symbols) plotted to coincide with universal compression data (open symbols) (Sanderson 1995). Empirical curve can be idealized as Eq. (1), where the failure strength slowly increases, in the ductile range, up to a maximum value of approximately 7.0 MPa for a strain rate of $10^{-3.55}$ s^{-1}, it remains constant in range of the transitional zone between $10^{-3.55}$ s^{-1} and $10^{-2.65}$ s^{-1}, and the fracture strength decreases slightly and keeps constant 4.5 MPa again in a brittle zone at higher strain rates.

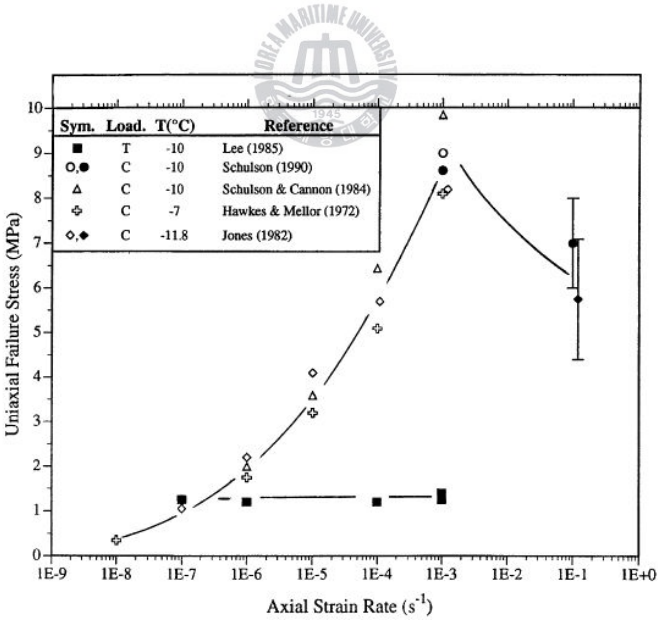

Fig. 2.2 Flow stress as a function of strain rate (Carney 2006, Schulson 1999, 2001)

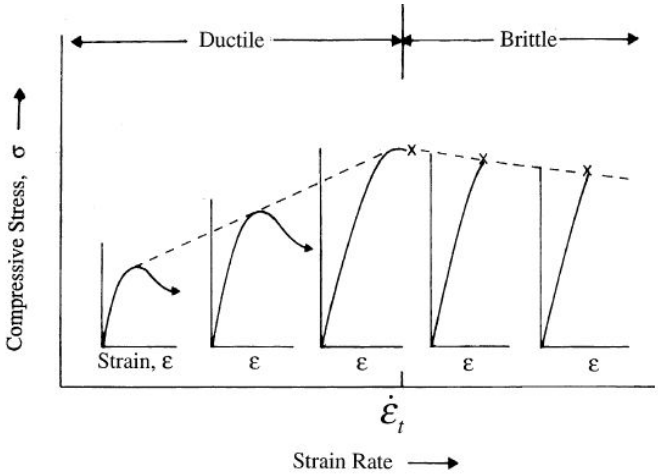

Fig. 2.3 Compressive failure modes in ice as a function of strain rate (Carney 2006, Schulson 1999, 2001)

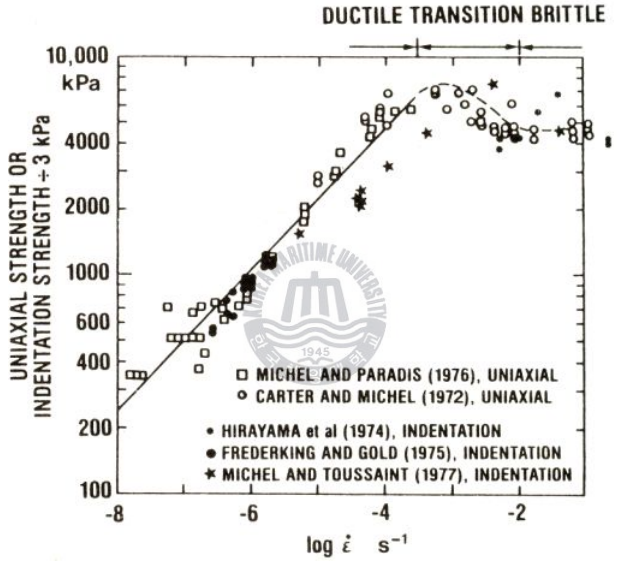

Fig. 2.4 Compressive uniaxial failure strength of S-2 ice according to strain rate (Ralston 1979)

$$\sigma_{cf} = \begin{cases} 10^{4.96} \times (\dot{\varepsilon})^{0.31406} & (\dot{\varepsilon} < 10^{-3.55}) \\ 7{,}000\,kPa & (10^{-3.55} \le \dot{\varepsilon} < 10^{-2.65}) \\ 7{,}720 - 322{,}100 \times \dot{\varepsilon} & (10^{-2.65} \le \dot{\varepsilon} < 10^{-2.0}) \\ 4{,}500\,kPa & (10^{-2.0} \le \dot{\varepsilon}) \end{cases} \quad (1)$$

3. Ice Mechanics and Simulation

Since time step size is usually controlled by the smallest element size over all elements in the full scale iceberg-ship collision simulation using explicit code, such as LS-DYNA, the modeling method of LNG carrier and iceberg is very important for the stable computation. Crushing of iceberg will be the most dominant in the ice failure under compressive stresses. Since the simulation of microscopic crushing failure is not suitable for full scale iceberg-ship collision problem using explicit analysis as mentioned before, macroscopic crushing failure mode is adopted for the simulation. For the understanding of macroscopic ice failure and its application to the simulation, two types, such as brittle and ductile behaviors, of unconfined uniaxial compressive strength tests of laboratory-grown fresh water ice specimens (Kim et al. 2007) were simulated. Indentation of level ice into a narrow structure was also simulated, whose results were compared with that of empirical formula.

Figure 3.1shows the experimental photograph of compression test ice specimen of brittle failure mode, and Fig. 3.2, its typical load curve (Kim et al. 2007). Figure 3.3illustrates the configuration of finite element mesh and dimension of ice specimen with two jigs, where its mesh size is 0.5 cm, bottom jig is fixed and top one, moving down. An elasto-plastic material with failure, MAT_PIECEWISE_LINEAR_PLASTICITY (MAT_24), was used for the uniaxial compressive strength simulation with equivalent compressive failure strength, and an elasto-plastic material with compressive and tensile yield stress-plastic strain curves, MAT_PLASTICITY_COMPRESSION_ TENSION (MAT_124), for the compressive strength simulation with separate compressive and tensile failure strength. Failure occurred with a single failure strain for both materials, and rate effect on the yield stress was neglected because of no significant strain rate sensitivity of ice in the rate range of iceberg-ship collision and uniaxial compressive strength tests. Material

properties of ice specimen of brittle failure mode are summarized in Table 3.1, and illustrated in Fig. 3.4, where ‘tension (0.1)’is referred to the elasto-plastic material together with consideration of compressive failure strength and tensile failure strength one tenth times of compressive one. MAT_124 was adopted for the examination of the distribution of tensile stress and its effects in the uniaxial compressive strength tests. Jigs were treated as elastic steel.

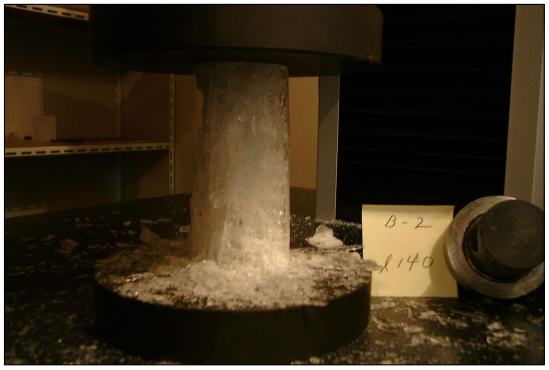

Fig. 3.1 Photograph of compression test ice specimen of brittle failure mode (Kim et al. 2007)

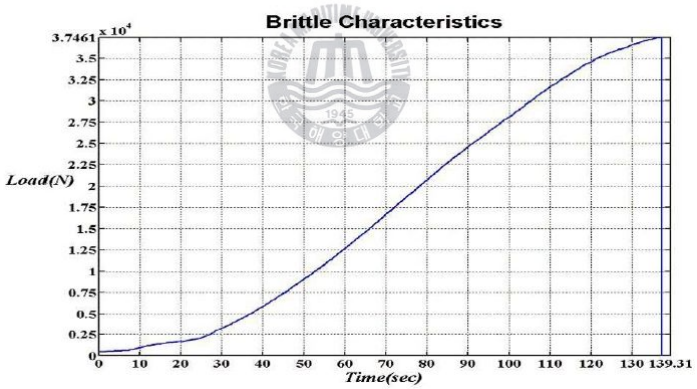

Fig. 3.2 Compression test ice specimen load of brittle failure mode (Kim et al. 2007)

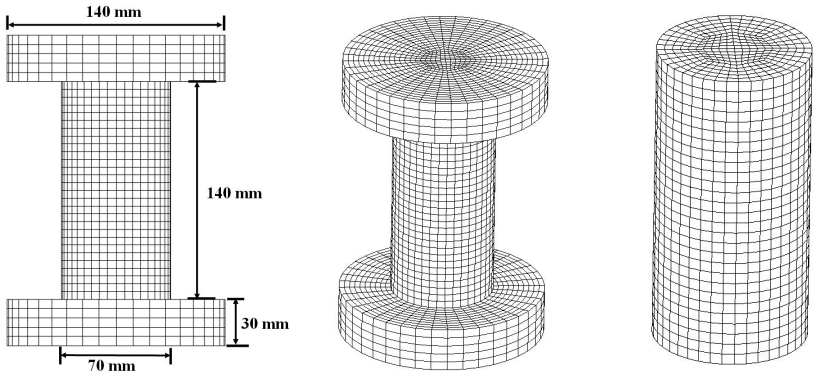

Fig. 3.3 Configuration of finite element mesh of compression test ice specimen of brittle failure mode

Table 3.1 Material properties of compression test ice specimen of brittle failure mode

Items \ Materials	Compression (MAT_24)	Tension (MAT_124)				
		(0.1)	(0.2)	(0.3)	(0.4)	(0.5)
Density (kg/m^3)	918.0	918.0				
Young modulus (GPa)	1.5	1.5				
Poisson's ratio	0.33	0.33				
Compressive yield stress (MPa)	9.0	9.0				
Compressive failure stress (MPa)	10.25	10.25				
Tensile yield stress (MPa)	0.0	- 0.9	- 1.8	- 2.7	- 3.6	- 4.5
Tensile failure stress (MPa)	0.0	- 2.15	- 3.05	- 3.95	- 4.85	- 5.75
Failure strain	0.007	0.007				

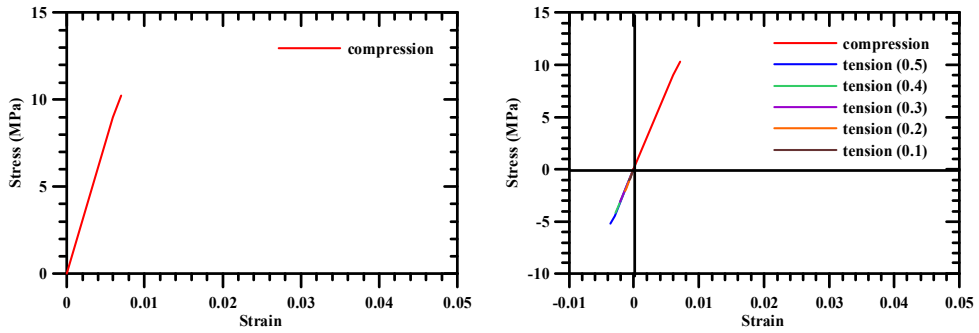

(a) MAT_24 (b) MAT_124

Fig. 3.4 Stress-strain curve for the simulation of compression test ice specimen of brittle failure mode

Figure 3.5(a) shows the configuration of compression test ice specimen failure simulation of brittle failure mode using MAT_24 at initial, ultimate and failure stages under constant compressive strain rate loading (loading velocity/specimen length) with the initial rate 1/5 times of constant one at initial stage, and Fig. 3.6(a), the failure configuration with its only failure part of finite element specimen. It can be found that its load curve is almost in good agreement with the test one, as shown in Fig. 3.7(a). Figures 3.5(b)～(f) and 3.6(b)～(f) exhibit the configurations and failure ones of ice specimen failure simulation with tensile failure stress using MAT_124 at failure stage, and it can be found that their failure configurations depend on the tensile failure stresses and become to the failure one of only compressive failure strength material using MAT_24 in Fig. 3.6(a) according to the increase of tensile failure strength, and that there is no change of their load curves regardless of tensile failure stresses and they are also in good agreements with the test one, as shown in Fig. 3.7(b).

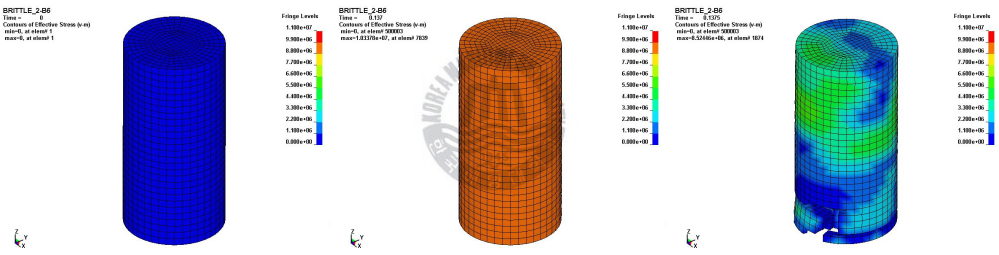

(a) MAT_24

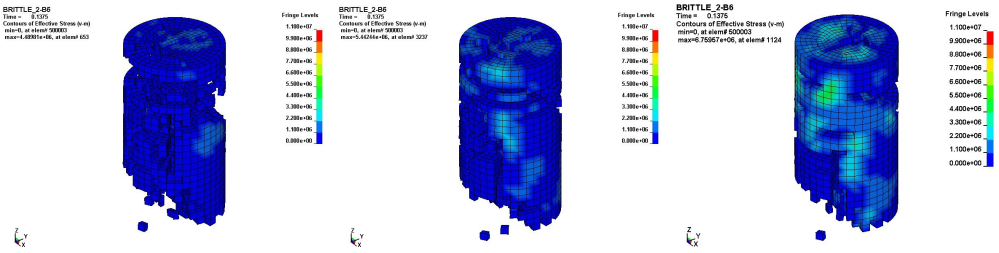

(b) MAT_124 tension (0.1) (c) MAT_124 tension (0.2) (d) MAT_124 tension (0.3)

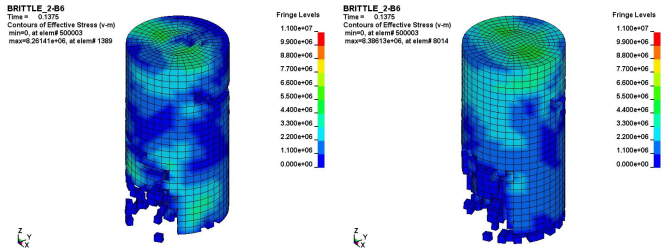

(e) MAT_124 tension (0.4) (f) MAT_124 tension (0.5)

Fig. 3.5 Total configurations of compression test ice specimen failure simulation in brittle failure mode

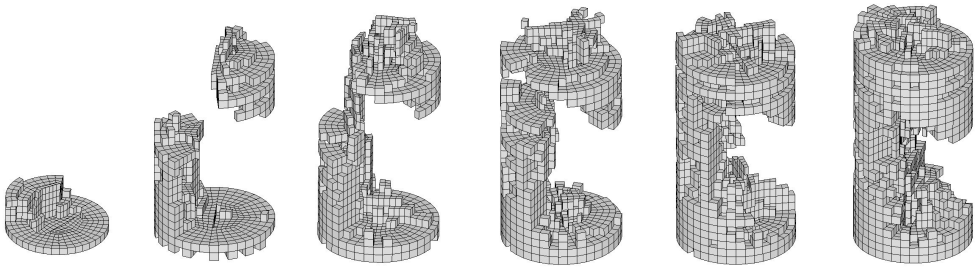

(a) compression (b) tension(0.5) (c) tension(0.4) (d) tension(0.3) (e) tension(0.2) (f) tension(0.1)

Fig. 3.6 Failure configurations of ice specimen failure simulation in brittle failure mode

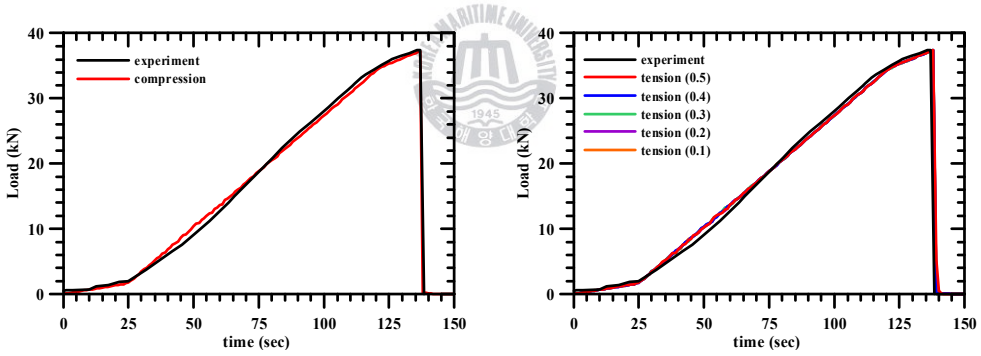

(a) MAT_24 (b) MAT_124

Fig. 3.7 Compression test ice specimen simulation load curves of brittle failure mode

From these responses, it can be inferred that tensile stress could be generated locally even under unconfined uniaxial compressive loading, its distribution is varied with its failure strength, and tensile failure strength is not

contributed to the compressive failure strength. Tensile stress might be generated locally through crack sliding in unconfined uniaxial compressive test ice specimen. From the applied stress-strain curve, Young's modulus, 1.5GPa, was not stiff compared to that the well known modulus, around 9.0GPa, of the general fresh water ice, and stress-strain curve showed very brittle mode.

As a brittle failure mode, Fig. 3.8 shows the experimental photograph of test ice specimen of ductile failure mode, and Fig. 3.9, its typical load curve (Kim et al 2007). Figure 3.10is the configuration of finite element mesh for the test ice specimen of ductile failure mode and its dimensions under the same boundary and loading conditions with those of brittle one. An elasto-plastic material with failure, MAT_PIECEWISE_LINEAR_ PLASTICITY (MAT_24), was used for the uniaxial compressive strength simulation. Material properties of ice specimen of ductile failure mode are summarized in Table 3.2, and illustrated in Fig. 3.11.

MAT_24 at initial, ultimate and plateau stage under constant compressive strain rate loading (loading velocity/specimen length) with the initial rate 1/5 times of constant one at initial stage. Macroscopic failure did not take place even at large strain in excess of 0.15, as shown in Figs. 3.12 and 3.13. It could be also found that its load curve is almost in good agreement with the test one, as shown in Fig. 3.14. The stress-strain curve was characterized by ascending and descending branches, and plastic strain in excess of 0.012 was imparted without macroscopic failure. Young's modulus was 0.95 GPa and ultimate stress, 6.225 MPa.

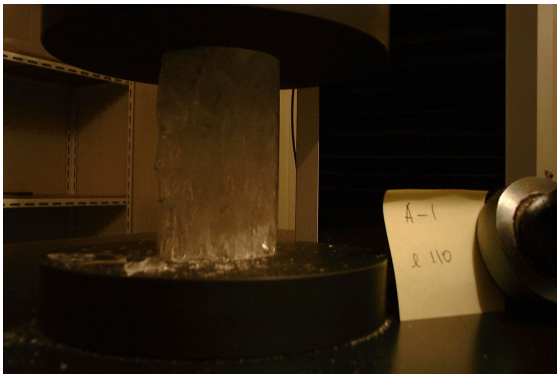

Fig. 3.8 Photograph of compression test ice specimen of ductile failure mode (Kim et al. 2007)

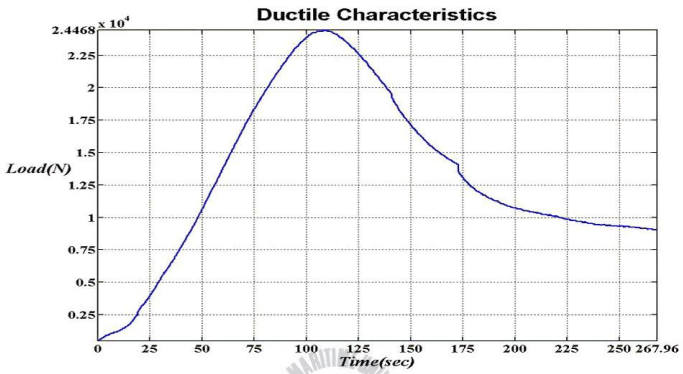

Fig. 3.9 Compression test ice specimen load curve of ductile failure mode

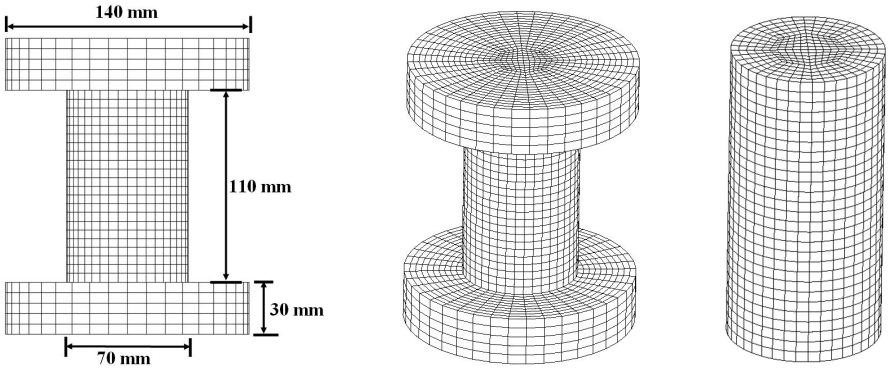

Fig. 3.10 Configuration of finite element mesh of compression test ice specimen of ductile failure mode

Table 3.2 Material properties of compression test ice specimen of ductile failure mode using MAT_24

Density (kg/m^3)	918.0
Young modulus (GPa)	0.95
Poisson's ratio	0.33
Yield stress (MPa)	6.000
Ultimate stress (MPa)	6.225

Plastic strain	0.0	0.0005	0.0018	0.014	0.034	0.054	0.094	0.104	0.114	0.124	0.134
Stress(MPa)	6.000	6.225	6.199	4.491	2.891	1.891	1.491	1.191	0.941	0.841	0.841

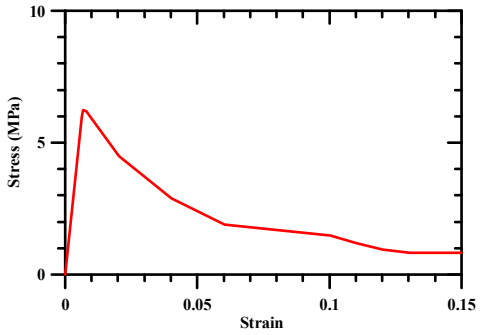

Fig. 3.11 Stress-strain curve for simulation of compression test ice specimen of ductile failure mode

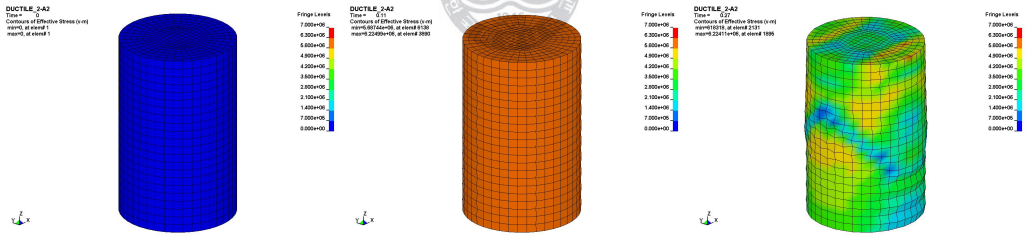

Fig. 3.12 Responses of compression test ice specimen failure simulation of ductile failure mode

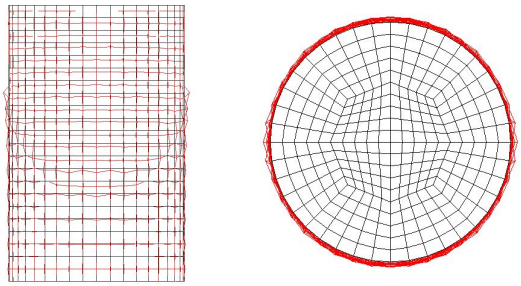

Fig. 3.13 Deformation of compression test ice specimen failure simulation of ductile failure mode

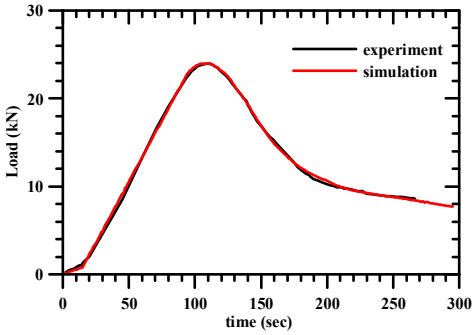

Fig. 3.14 Compression test ice specimen simulation load curves of brittle failure mod

4. Collision Scenarios and Simulation Models

FSI (Fluid-Structure Interaction, referred to 'FSI' forward) analysis technique with consideration of surrounding sea water was used in this study for full scale iceberg-ship bow shoulder collision simulations. Figure 4.1 shows the overall finite element configurations of full scale iceberg-ship collision simulations with cubic iceberg without air part using FSI analysis technique and their zoom view. Full scale iceberg-ship bow shoulder collision simulations were carried out with 2.0knots drift speed of iceberg and 15.0 knots speed, as shown in Fig. 4.2, and 70 degree attack angle of iceberg was considered in this study. Cubic iceberg (20×20×20 m in length, width and height with 2.07 meter height above waterline) was considered, as shown in Fig. 4.3, with volume and weight, 8,000 m3 and 7,344 ton. Total finite element meshes generally consist of two parts, such as total rigid part and deformed one, where the former part is constrained with fluid and air Eulerian domain in FSI analysis technique. The mesh size of shell element in deformed ship and solid one in iceberg is around 0.5 meter. The numbers of their finite elements are summarized in Table 4.1. Around 0.5 m was chosen as the standard mesh size of iceberg, and 2 more types of mesh size were considered, such as 0.25 and 1.00 m, for the consideration of the effect of iceberg modeling on the iceberg crushing strength.

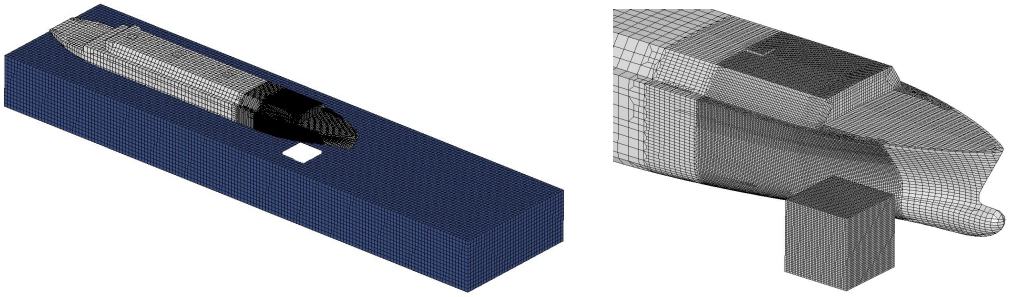

Fig. 4.1 Finite element configurations of full scale iceberg-ship collision simulation using FSI analysis technique

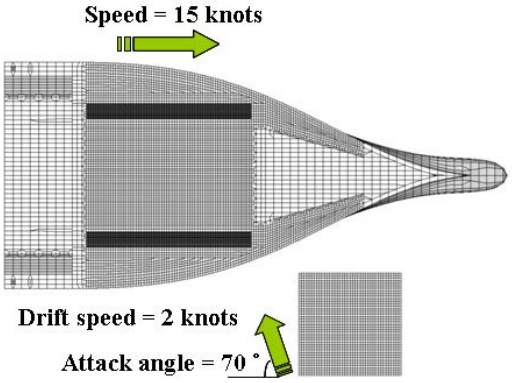

Fig. 4.2 Full scale iceberg-ship collision scenarios of LNG carrier with cubic iceberg

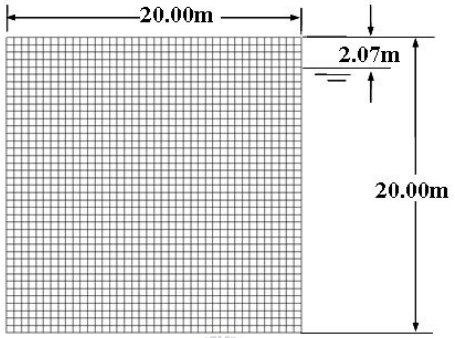

Fig. 4.3 Finite element configuration and dimension of cubic iceberg

Table 4.1 Number and type of finite element in modeling

part		element type	No. of element
ship	rigid part	shell	4,380
	Deformed part	shell	127,170
		beam	58,160
iceberg	cube (20×20×20 m)	solid	64,000

Iceberg will exhibit brittle behavior at relative high deformation rates in the range around 5×10^{-2} s^{-1} to 100 s^{-1}, under the iceberg-ship collision simulation with LNG carrier speed 15.0 knots and iceberg drifting speed 2.0 knots. It can be seen from Fig. 4.4 that failure peak stress of iceberg is much larger than that of sea ice in the brittle region (Han et al. 2007). Compressive crushing

failure stress of iceberg was raised to 8.0 MPa as a standard one of ice type iceberg in this study. In addition to the crushing failure strength of iceberg, its failure strain would be also important factor for the iceberg crushing strength, as mentioned in Chapter 3. Its stress-strain curves are shown in Fig. 4.5 according to failure strains 0.01, 0.03, 0.05 and 0.10, where failure strain 0.10 was chosen as a standard one for the full scale iceberg-ship collision simulation. The effects of Young's modulus and failure stress on the collision responses were also examined, where Young's modulus 2.0, 4.0 and 8.0 GPa were considered with same yield stress 6.4 MPa, failure stress 8.0 MPa and failure strain 0.01, as shown in Fig. 4.6, and failure stress 4.5 and 8.0 MPa according to failure strain 0.01, 0.05 and 0.10, with the same rate of yield stress to failure stress 3.6 and 6.4 MPa, respectively, as shown in Fig. 4.7. Contrary to the compression test ice specimen failure simulation of brittle failure mode considering failure tensile stress with failure compression stress in Chapter 3, iceberg crushing strength might be influenced by the failure tensile stress. The effect of failure tensile stress with a fifth times strength of failure compressive stress 8.0 MPa according to failure strain 0.01 and 0.10 were considered. The total scenarios of full scale iceberg-ship collision are summarized in Table 4.2, which might include most of the interested and important factors for the collision responses, and each scenario is assigned to its own case number for convenience.

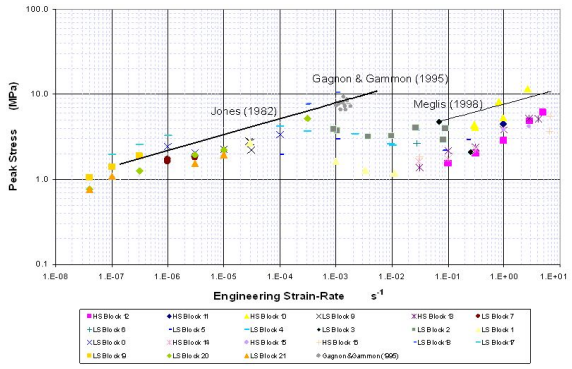

Fig. 4.4 Peak stress of iceberg according to strain rate (IOC/NRC)

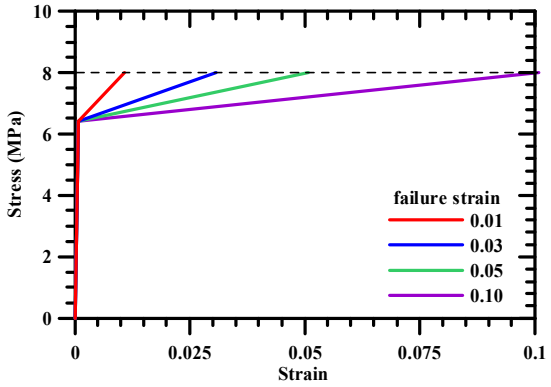

Fig. 4.5 Stress-strain curve of iceberg according to failure strain 0.01, 0.03, 0.05 and 0.10

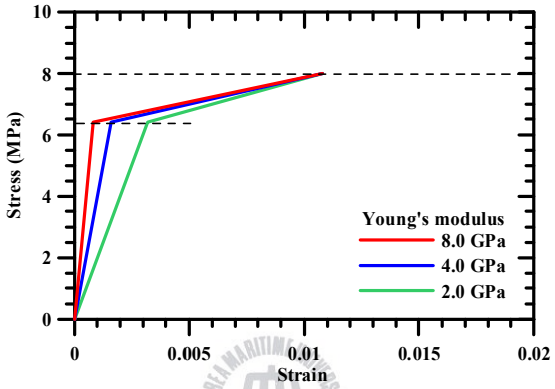

Fig. 4.6 Stress-strain curve of iceberg according to Young's modulus

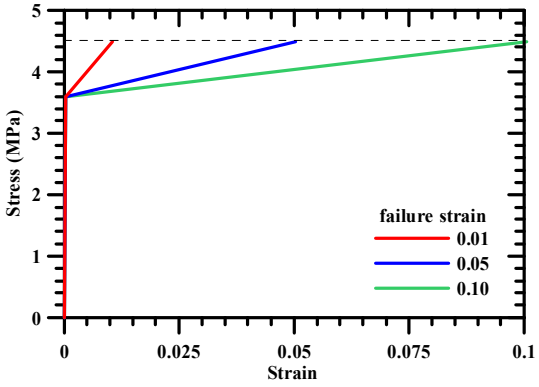

Fig. 4.7 Stress-strain curve of iceberg with failure stress 4.5 MPa according to failure strain 0.01, 0.05 and 0.10

Table 4.2 Scenarios of full scale iceberg-ship collision

scenario type	Iceberg (Density 918.0 kg/m3, Poisson's ratio 0.33)				Case
	failure strain	Young's modulus	Failure stress	mesh size	
5.1 failure strain	0.01	8.0 GPa	8.0 MPa (C)	0.50 m	Case 1
	0.03				Case 2
	0.05				Case 3
	0.10				Case 4
5.2 Young's modulus	0.01	2.0 GPa	8.0 MPa (C)	0.50 m	Case 5
		4.0 GPa			Case 6
		8.0 GPa			Case 1
5.3 failure stress	0.01	8.0 GPa	8.0 MPa (C)	0.50 m	Case 1
	0.05				Case 3
	0.10				Case 4
	0.01	8.0 GPa	4.5 MPa (C)	0.50 m	Case 7
	0.05				Case 8
	0.10				Case 9
5.4 failure tension	0.01	8.0 GPa	8.0 MPa (C)	0.50 m	Case 1
	0.10				Case 4
	0.01	8.0 GPa	8.0 MPa (+0.2T)	0.50 m	Case 10
	0.10				Case 11
5.5 iceberg mesh size	0.01	8.0 GPa	8.0 MPa (C)	0.25 m	Case 12
				0.50 m	Case 1
				1.00 m	Case 13

In addition to the performance of full scale iceberg-ship collision simulations, structural safety assessment of MARK III membrane type CCS is important subject and also the objective of collision simulation. Structural safety assessment of CCS was carried out at the location of maximum deformation in the inner hull by the local zooming analysis technique. All expected locations of maximum deformation in the inner hull were set as the segments of local zooming analysis for the structural safety assessment of MARK III membrane type CCS in every case of iceberg-ship collision simulation, as shown in Fig. 4.8. Maximum deformation and acceleration usually occurred in the inner hull around at intersecting point of web and stringer.

Figure 4.9 illustrates the local zooming analysis model, where 2 pieces of

MARK III CCS are attached to the segment by merging mastic to the inner hull segment. The information and/or characteristics of damage between mastic and inner hull plate by the impact could be very important factors of the structural safety assessment of MARK III membrane CCS. In this study, however, this information has been not yet figured out and components of CCS were treated by the orthotropic and isotropic elastic materials, as shown in Table 4.3. Therefore, the qualitative results could be obtained from this structural safety assessment. The size of each piece of MARK III CCS is 3×1 meters in width and height.

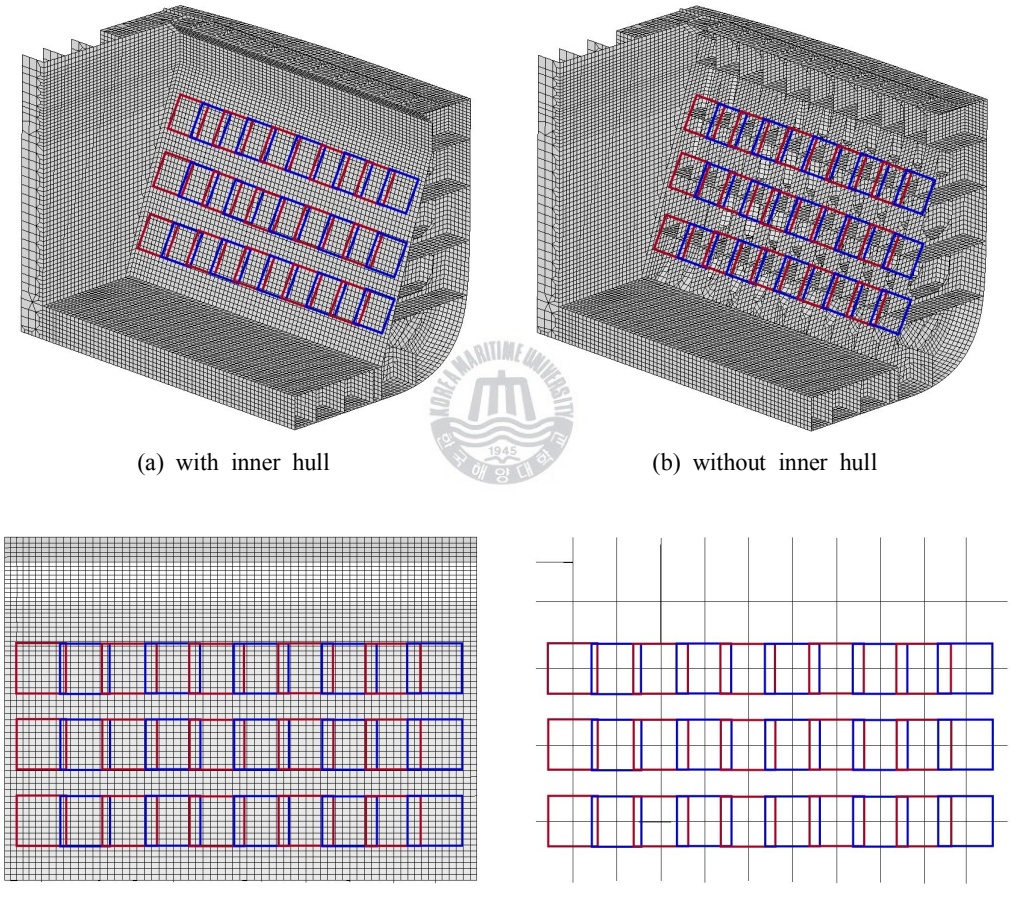

(a) with inner hull (b) without inner hull

(c) Front view with inner hull (d) Front view without inner hull

Fig. 4.8 Configuration of segments in inner hull for local zooming analysis

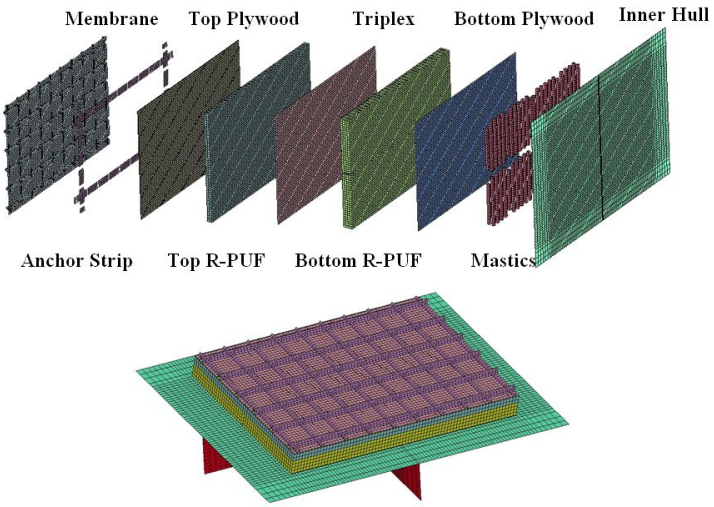

Fig. 4.9 Local zooming analysis model of MARK III membrane type CCS

Table 4.3 Material properties of MARK III membrane type CCS specimen (Lee et al. 2008)

	plywood	R-PUF	triplex	mastic	membrane	steel
E(n)(MPa)	8,900	142	13,133	2,934	200,000	206,000
E(s)(MPa)	7,500	142	-	-	-	-
E(t)(MPa)	520	84	-	-	-	-
Nu(ns)	0.17	0.24	0.3	0.3	0.27	0.3
Density	7.10E-10	1.25E-10	2.50E-09	1.50E-09	7.85E-09	7.85E-09
Model	Solid,Shell/Ortho	Solid/Ortho	Shell/Iso	Solid/Iso	Shell/Iso	Shell/Iso

5. Full-Scale Iceberg-Ship Collision Simulation

In the following sections, diverse collision simulation parameters were examined on the effects of damage responses according to the full-scale iceberg-ship collision simulation scenarios in Table 4.2 with 20×20×20 m cubic ice type iceberg, 0.5 m finite element size, 8.0 GPa Young's modulus, 70 degree attack angle, analysis techniques FSI and no consideration of inner fluid, using collision damage configurations and responses of LNG carrier and iceberg. Damage configurations were compared with each case, such as plastic strain and effective stress distributions of the side structure, plastic strain, effective stress, the maximum deformation and acceleration distributions in the inner hull, and damage configuration of ice type iceberg. Several responses were also compared with each case, such as collision force, absorbed energy, the maximum deformation and acceleration of inner hull, and vertical displacement of iceberg. Some of damage configurations and responses were illustrated in this paper because of limited space, and the maximum values of all responses in each case were summarized in Table 5.1. Iceberg would be crushed depending on full-scale iceberg-ship collision simulation scenarios in Table 4.2, and its failure element numbers and its ratio of failure elements to total ones in each case were also summarized in Table 5.1. Figure 5.1 shows the realistic configurations of LNG carrier collision simulation with cubic iceberg with and without surrounding fluid using FSI analysis technique.

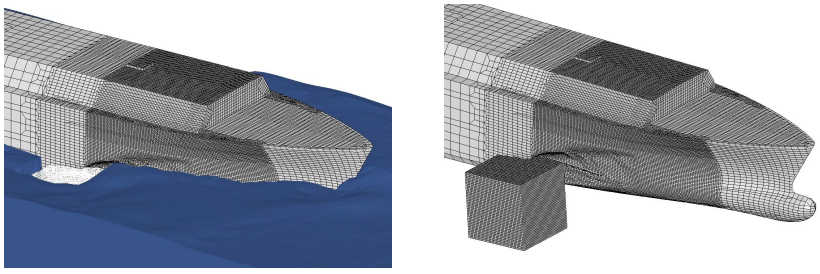

with surrounding fluid　　without surrounding fluid

Fig. 5.1 Collision configuration of cubic iceberg using FSI analysis technique

Table 5.1 Summaries of the maximum values of responses and iceberg failure ratios in each case

Case	collision force (MN)	LNGC	iceberg		inner hull		iceberg		
		absorbed energy (MJ)	absorbed energy (MJ)	vertical displ. (m)	max. deform. (m)	max. accel. (m/s^2)	total number	failure number	ratio (%)
1	56.60	309.45	0.67	5.62	0.039	2,125.30	64,000	2,765	4.32
2	69.53	397.64	2.02	6.57	0.043	2,453.68	64,000	2,093	3.27
3	62.98	467.12	4.37	6.98	0.059	2,818.48	64,000	1,770	2.77
4	81.07	571.13	8.05	7.21	0.097	3,916.80	64,000	1,171	1.83
5	48.70	271.26	0.98	5.28	0.044	2,396.77	64,000	3,036	4.74
6	50.29	297.87	0.69	5.58	0.039	2,325.74	64,000	2,916	4.56
7	62.58	171.45	0.58	6.24	0.044	1,800.01	64,000	3,815	5.96
8	68.54	310.65	2.99	8.63	0.047	2,577.76	64,000	2,465	3.85
9	75.79	404.31	5.17	9.90	0.059	2,901.64	64,000	1,772	2.77
10	51.40	235.88	0.88	5.15	0.041	2,194.21	64,000	2,859	4.47
11	73.73	514.92	6.36	7.45	0.069	2,881.66	64,000	1,414,	2.21
12	39.30	60.35	0.54	5.95	0.025	1,917.04	512,000	17,855	3.49
13	112.20	934.99	3.13	5.35	0.144	4,150.30	8,000	318	3.98

5.1 Response of collision simulation according to failure strain of iceberg

Crushing strength of iceberg is one of the most important factors for the crashworthiness of LNG carrier in the iceberg-ship collision simulation, and its failure strain might influence its crushing strength. In this section, the effect of iceberg failure strain on the responses of full scale iceberg-LNG carrier collision simulation was considered, such as 0.01, 0.03, 0.05 and 0.10, as shown in the first scenario of Table 4.2. The collision damage configurations of side structure and inner hull of LNG carrier and iceberg according to iceberg failure strains 0.01, 0.03, 0.05 and 0.10 are illustrated in Figs. 5.2-5.4, respectively, and their responses, in Fig. 5.5. Their maximum values of responses and iceberg failure ratios were summarized in Cases 1-4 of Table 5.1.

Failure strain of iceberg had an influence on its crushing strength and the collision responses of LNG carrier. With increase of failure strain, iceberg was

crushed less and less, and the collision damages of the side structure and the deformation in the inner hull occurred gradually larger. Their responses were also increased more or less gradually according to failure strain, and their relative differences of responses between failure strain 0.10 and the others 0.05, 0.03 and 0.01 were more or less large.

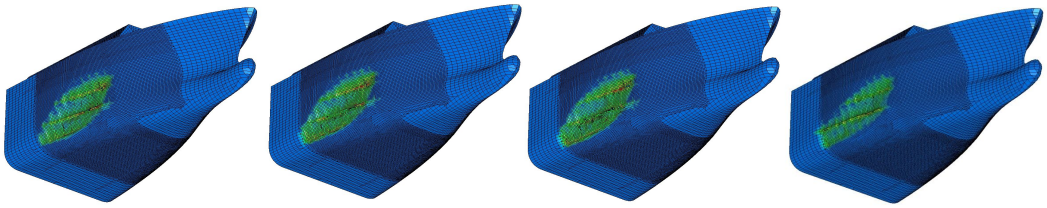

(a) 0.01 (b) 0.03 (c) 0.05 (d) 0.10

Fig. 5.2 Collision damage configuration of side structure according to failure strain (plastic strain)

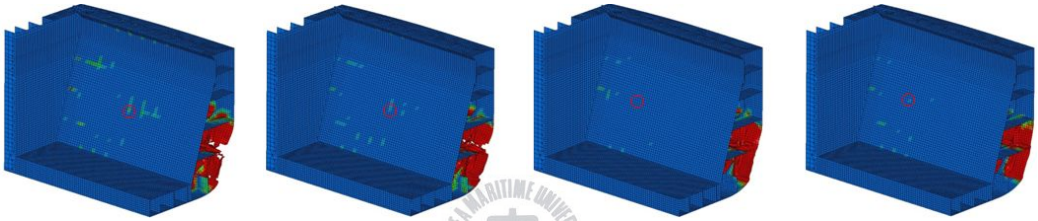

(a) 0.01 (b) 0.03 (c) 0.05 (d) 0.10

Fig. 5.3 Collision damage configuration of inner hull at maximum deformation according to failure strain (plastic strain)

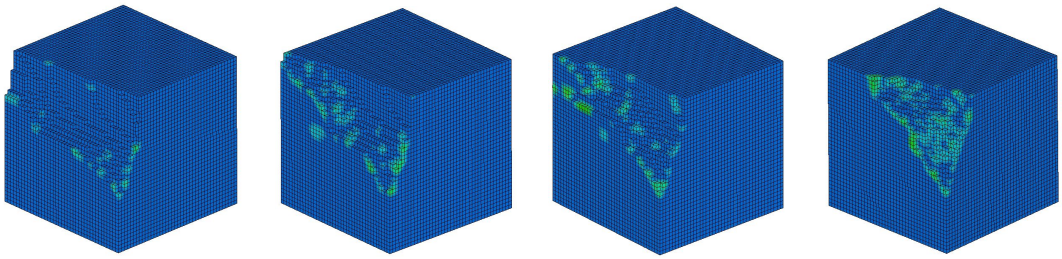

(a) 0.01 (b) 0.03 (c) 0.05 (d) 0.10

Fig. 5.4 Collision damage configuration of ice type iceberg with LNG carrier according to failure strain

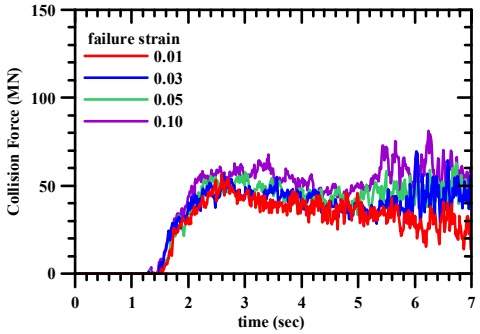

(a) Collision force

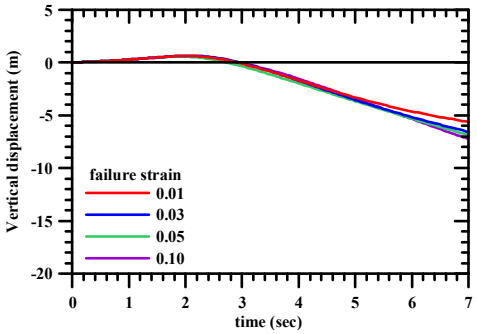

(b) Vertical displacement of iceberg

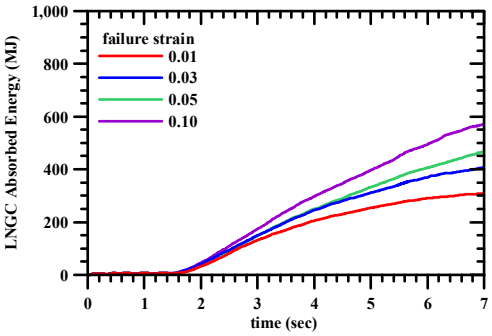

(c) LNGC absorbed energy

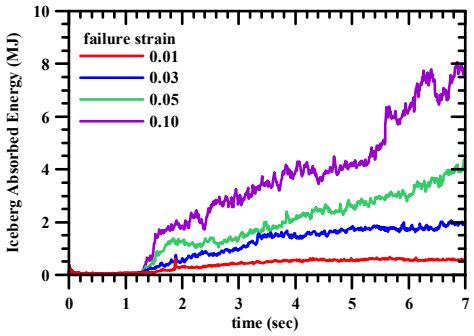

(d) Iceberg absorbed energy

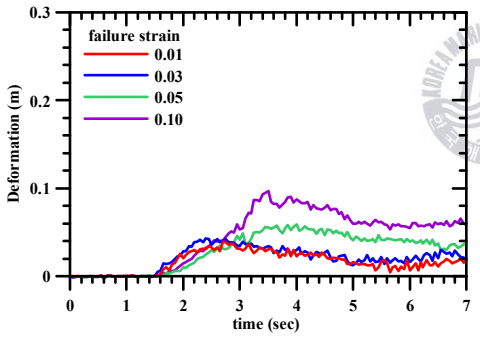

(e) Maximum deformation on inner hull

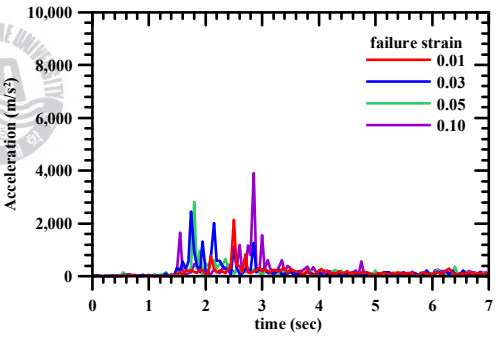

(f) Maximum acceleration on inner hull

Fig. 5.5 Response of collision simulation according to failure strain

5.2 Response of collision simulation according to Young's modulus of iceberg

Young's modulus of iceberg would be important factor for its crushing strength. In this section, the effect of iceberg Young's modulus on the

responses of full scale iceberg-LNG carrier collision simulation was considered, such as 2.0, 4.0 and 8.0 GPa, as shown in the second scenario of Table 4.2 and stress-strain curve of Fig. 4.6 using failure strain 0.01. The collision damage configurations of side structure and inner hull of LNG carrier and iceberg with iceberg Young's modulus 8.0 GPa were already illustrated in Figs. 5.2-5.4(a), and those configurations with iceberg Young's modulus 2.0 and 4.0 GPa, in Figs. 5.6-5.8(a, b), respectively. Their maximum values of responses and iceberg failure ratios were also summarized in Cases 5-6 of Table 4.2.

It could be found, contrary to expectation, that Young's modulus of iceberg did not have an influence on its crushing strength and the collision responses, such as the damage configuration of side structure and the maximum deformation and acceleration responses in the inner hull.

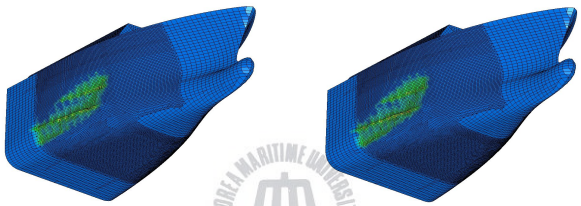

(a) 2.0 GPa (b) 4.0 GPa

Fig. 5.6 Collision damage configuration of side structure according to Young's modulus (plastic strain)

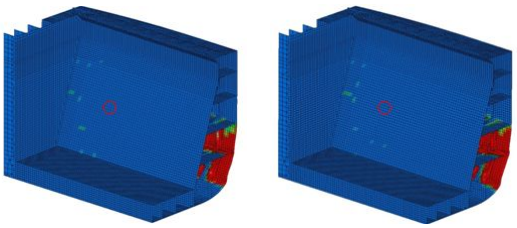

(a) 2.0 GPa (b) 4.0 GPa

Fig. 5.7 Collision damage configuration of inner hull at maximum deformation according to Young's modulus (plastic strain)

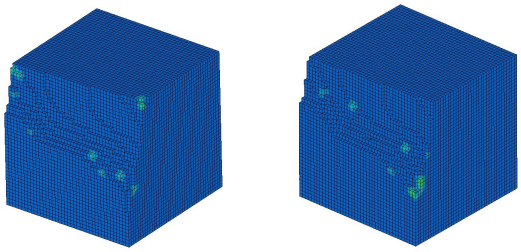

(a) 2.0 GPa (b) 4.0 GPa

Fig. 5.8 Collision damage configuration of ice type iceberg with LNG carrier according to Young's modulus

5.3 Response of collision simulation according to failure stress of iceberg

In addition to the failure strain of iceberg, failure stress could be an important factor for its crushing strength. In this section, the effect of its failure stress on the responses of full scale iceberg-LNG carrier collision simulation was considered, such as 4.5 and 8.0 MPa, according to failure strains 0.01, 0.05 and 0.10, as shown in the third scenario of Table 4.2 and Figs. 4.5 and 4.7. The collision damage configurations of side structure and inner hull of LNG carrier and iceberg using iceberg failure stress 8.0 MPa were already illustrated in Figs. 5.2-5.4(a, c, d) for failure strain 0.01, 0.05 and 0.10, respectively. Their configurations using iceberg failure stress 4.5 MPa according to failure strains 0.01, 0.05 and 0.10 are shown in Figs. 5.9-5.11, and their maximum values of responses and iceberg failure ratios were also summarized in Cases 7-9 of Table 4.2.

As mentioned before in the case of failure stress 8.0 MPa in Section 5.1, failure strain of iceberg had an influence on the crushing strength of iceberg and the collision responses, such as the damages of the side structure and the responses of the maximum deformation and acceleration in the inner hull. For the case of failure stress 4.5 MPa, the general trends of the collision damages and responses according failure strain were almost the same as those of the case of failure stress 8.0 MPa. Iceberg in the case of failure stress 4.5 MPa

was crushed a little bit more than that of the case of failure stress 8.0 MPa, therefore the collision damages and responses of the former case generally showed a little bit smaller than those of the latter case. It could be found that failure stress of iceberg had a slight influence on the collision responses, and the difference of responses in the inner hull for the failure stresses 4.5 and 8.0 MPa increased with increase of failure strain.

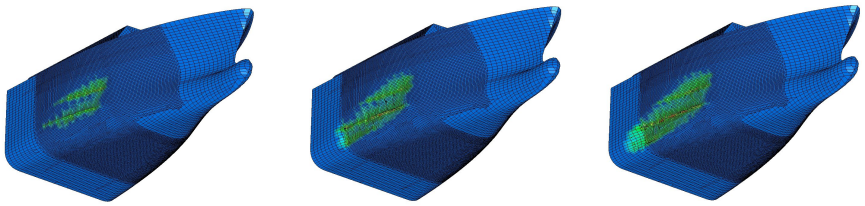

(a) 0.01 (c) 0.05 (d) 0.10

Fig. 5.9 Collision damage configuration of side structure of failure strength 4.5 MPa according to failure strain (plastic strain)

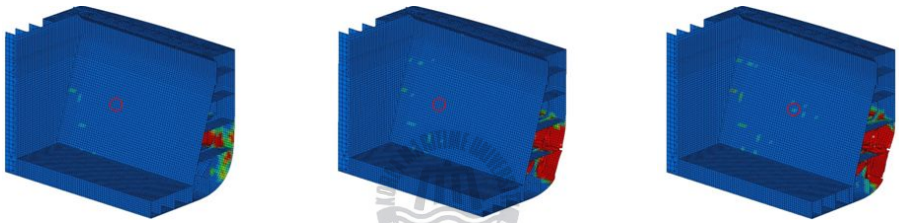

(a) 0.01 (c) 0.05 (d) 0.10

Fig. 5.10 Collision damage configuration of inner hull at maximum deformation of failure strength 4.5 MPa according to failure strength (plastic strain)

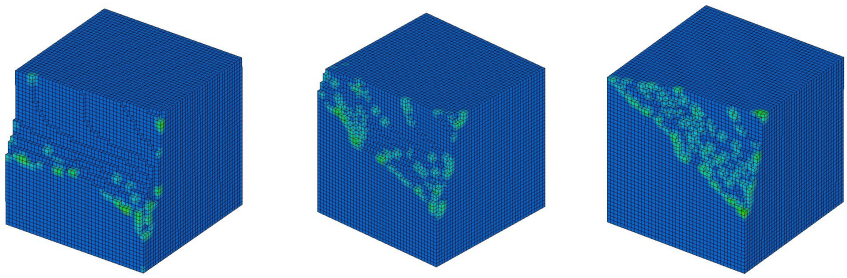

(a) 0.01 (b) 0.05 (c) 0.10

Fig. 5.11 Collision damage configuration of ice type iceberg with LNG carrier of failure strength 4.5 MPa according to failure strain

5.4 Response of collision simulation according to failure tensile stress of iceberg

As examined in Chapter 3 about the effect of failure tensile stress of compressive ice test specimen simulation on its crushing strength in the brittle range, the failure tensile stress with a fifth times strength of failure compressive stress 8.0 MPa of iceberg was considered together with the latter for the examination of its effect on the responses of full scale iceberg-LNG carrier collision simulation for failure strain 0.01 and 0.10, as shown in the fourth scenario of Table 4.2. Failure tensile stress with a fifth times strength of failure compressive stress will be also referred to 'tension (0.2)' for convenience as in Chapter 3. The collision damage configurations of the side structure and inner hull of LNG carrier and iceberg using only failure compressive stress 8.0 MPa of iceberg were already illustrated in Figs. 5.2-5.4(a, d) for failure strain 0.01 and 0.10, respectively, and their responses of collision simulation, in Fig. 5.5. The damage configurations of the side structure and inner hull with iceberg failure tensile stress, 'tension (0.2)', for the failure strain 0.01 and 0.10 are shown in Figs. 5.12-5.14(a, b), respectively, and their maximum values of responses and iceberg failure ratios were also summarized in Cases 10-11 of Table 4.2.

As expected, the general collision damage configurations and responses of the side structure and inner hull in the case of 'tension (0.2)'were similar to those of no consideration of failure tensile stress according to failure strains 0.01 and 0.10. Contrary to no effect of failure tensile stress of compressive ice test specimen simulation on its crushing strength in the brittle range, the failure tensile stress of iceberg had a very slight influence on the crushing strength of iceberg and the collision damages of the side structure and responses in the inner hull. While the responses of the maximum deformation and acceleration in the inner hull in the case of no consideration of failure tensile stress occurred a little bit larger than those of tension (0.2)' in the case failure strain

0.10, the collision damages of the side structure in the former case, a little bit larger than those of the latter case in the case of failure strain 0.01. Therefore, the difference of responses in the innerhull according to failure strains 0.01 and 01.0 became a little bit smaller compared to that of no consideration of failure tensile stress.

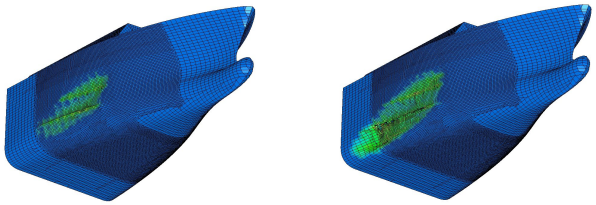

(a) 0.01 (b) 0.10

Fig. 5.12 Collision damage configuration of side structure according to failure strain with consideration of tension (0.2) (plastic strain)

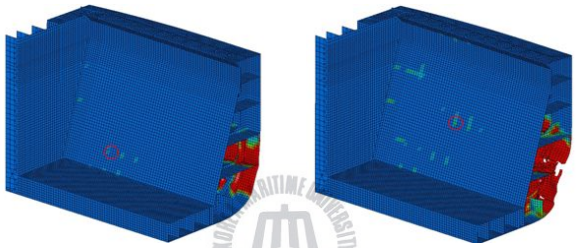

(a) 0.01 (b) 0.10

Fig. 5.13 Collision damage configuration of inner hull at maximum deformation according to failure strain with consideration of tension (0.2) (plastic strain)

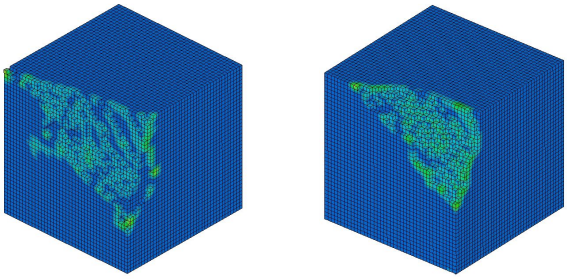

(a) 0.01 (b) 0.10

Fig. 5.14 Collision damage configuration of ice type iceberg with LNG carrier according to failure strain with consideration of tension (0.2)

5.5 Response of collision simulation according to mesh size of iceberg

Iceberg mesh size could influence the collision responses of LNG carrier. Iceberg mesh size 0.50 m is almost the same one as that of the deformed LNG carrier. In this section, the effect of iceberg mesh size on the responses of full scale iceberg-LNG carrier collision simulation was considered, such as iceberg mesh sizes 0.25, 0.50 and 1.00 m, as shown in the fifth scenario of Table 4.2. The collision damage configurations of side structure and inner hull of LNG carrier and iceberg for the case of iceberg mesh size 0.50 m were already illustrated in Figs. 5.2-5.4(d). The damage configurations for the cases of iceberg mesh sizes 0.25 and 1.00 m are shown in Fig. 5.15-5.17(a, b), respectively, and their responses of collision simulation, in Fig. 5.18. Their maximum values of responses and iceberg failure ratios were also summarized in Cases 12-13 of Table 4.2.

Mesh size of ice type iceberg modeling had a great influence on its crushing strength and the collision responses, such as the damages of side structure and the maximum deformation and acceleration responses in the inner hull. While the collision damages of the side structure occurred more and more severely with increase of iceberg mesh size, their responses in the inner hull were almost the same for the mesh sizes 0.25 and 0.5 m but much smaller than those of mesh size 1.0 m. Iceberg mesh sizes 0.25 and 1.00 m are an half and twice side length of mesh size 0.50 m in the side structure, and seemed to have relatively much smaller and larger crushing strengths compared to its mesh size 0.5 m, respectively. Mesh size of iceberg should be considered together with its materials for the reasonable iceberg modeling.

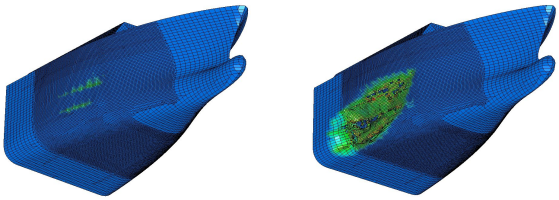

(a) 0.25m (b) 1.00m

Fig. 5.15 Collision damage configuration of side structure according to iceberg mesh size (plastic strain)

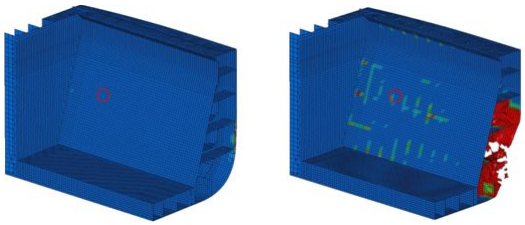

(a) 0.25m (b) 1.00m

Fig. 5.16 Collision damage configuration of inner hull at maximum deformation according to iceberg mesh size according (plastic strain)

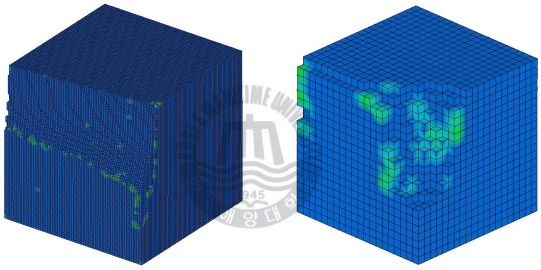

(a) 0.25m (b) 1.00m

Fig. 5.17 Collision damage configuration of ice type iceberg with LNG carrier to iceberg mesh size

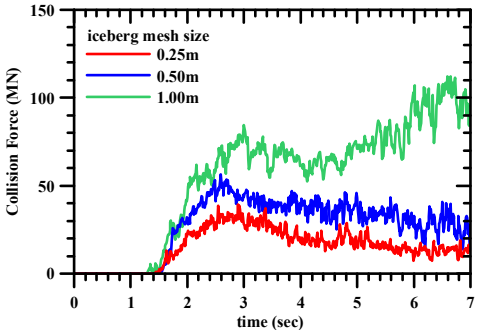

(a) Collision force

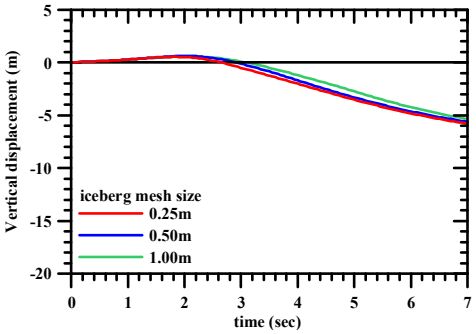

(b) Vertical displacement of iceberg

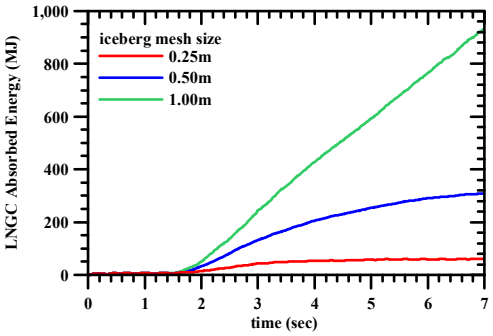

(c) LNGC absorbed energy

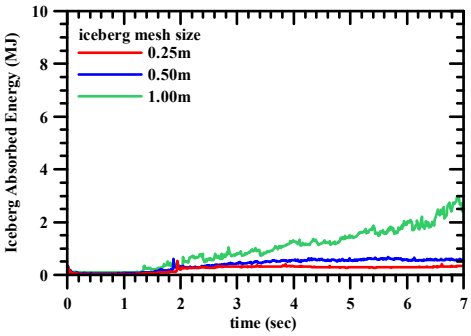

(d) Iceberg absorbed energy

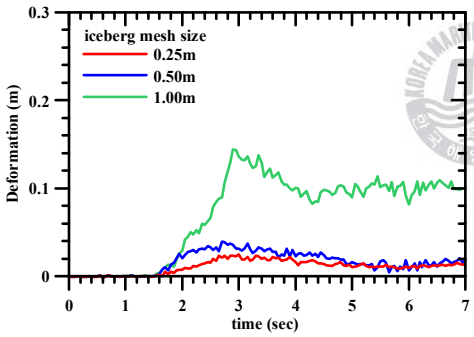

(e) Maximum deformation on inner hull

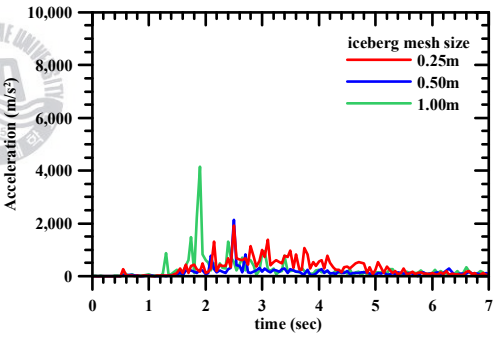

(f) Maximum acceleration on inner hull

Fig. 5.18 Response of collision simulation according to iceberg mesh size

6. Structural Safety Assessment of CCS

Structural safety assessments of MARK III membrane type CCS were carried out by local zooming analysis of the segments at the location of the maximum deformation in the inner hull in the cases of 20×20×20 m cubic iceberg with failure strain 0.01 and 0.10 and 30×30×30 m cubic one with failure strain 0.10, and in the case of 70 degree angle of blow with analysis technique FSI. Figure 6.1 shows the 20 times enlarged deformation configurations of inner hull, and Figs. 6.2 and 6.3, their responses in the inner hull at maximum acceleration and deformation, respectively, where the maximum global deformations were 39.2 and 96.9mm in the cases of failure strain 0.01 and 0.10 of 20×20×20 m cubic iceberg, respectively, and 208.8mm in the case of failure strain 0.10 of 30×30×30 m one.

(a) failure strain 0.01 (20×20×20m) (b) failure strain 0.10 (20×20×20m)

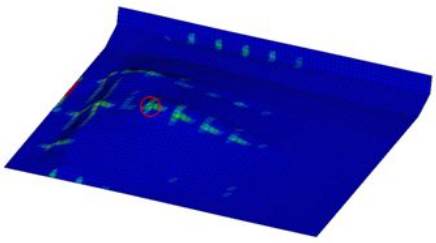

(c) failure strain 0.10 (30×30×30m)

Fig. 6.1 Collision damage configuration of inner hull at maximum deformation with analysis technique FSI

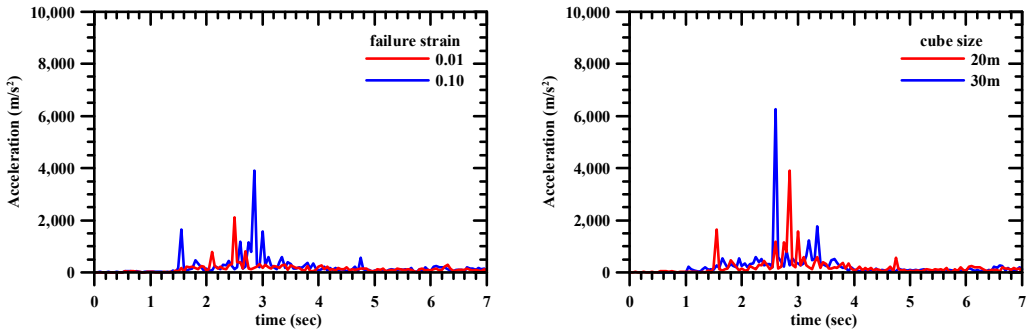

(a) 20×20×20m cubic iceberg (b) failure strain 0.10

Fig. 6.2 Response of collision simulation on the inner hull at maximum acceleration with analysis technique FSI

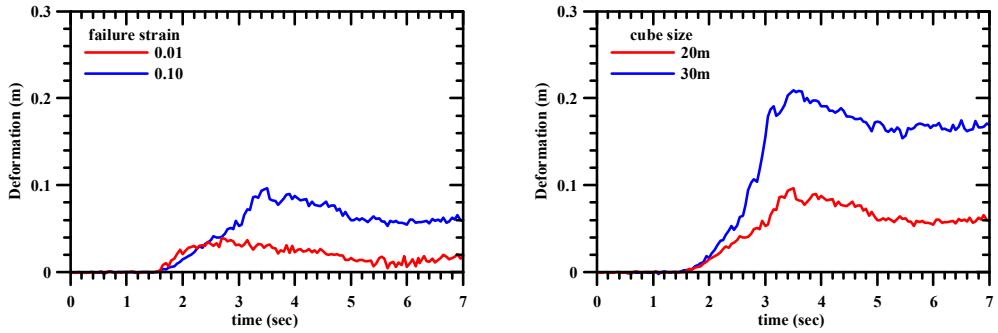

(a) 20×20×20m cubic iceberg (b) failure strain 0.10

Fig. 6.3 Response of collision simulation on the inner hull at maximum deformation with analysis technique FSI

Contrary to the case of NO96 CCS, safety assessment criterion for the deformation of MARK III membrane type CCS has not yet been known. However, its safety assessment criterion for the strength was suggested, such as the minimum specified ultimate strength of CCS component materials, as shown in Table 6.1, where the maximum normal tensile/compressive stress and shear stress were evaluated with the ultimate strength of material in each orientation for polyurethane form and plywood layers, and maximum von Mises stress, with the ultimate strength of mastic (Kwon 2008, ABS 2006).

Figure 6.4 illustrates the local deformation configurations of segments with mastics, which were magnified by scale factor 50, and the locations of the local maximum deformations were indicated by the red circles. While the

maximum global deformation was measured as the relative difference between the maximum and minimum displacements in the whole inner hull, the maximum local one, in the segment. This maximum local deformation will be the basis of the allowable deformation criterion of MARK III membrane type CCS. Figure 6.5 shows their responses of the local maximum deformations in the inner hull together with its global ones, where their local deformations were 5.56 and 8.32 mm in the cases of failure strain 0.01 and 0.10 of 20×20×20 m cubic iceberg, respectively, and 32.6 mm in the case of failure strain 0.10 of 30×30×30 m one, respectively.

Table 6.1 Ultimate strength of polyurethane form, plywood and mastic (ABS 2006)

Material (20˚C)	Orientation of Grade	Strength (MPa)
Polyurethane Form (PUF)	Horizontal Tension	2.4
	Horizontal Compression	2.4
	Vertical Tension	1.4
	Vertical Compression	2.0
	Shearing	1.4
Plywood	Horizontal Tension	40.0
	Horizontal Compression	40.0
	Vertical Tension	2.0
	Vertical Compression	20.0
	Shearing	2.8
Mastic	Von Mises	15.0
Steel	Steel(Mild)	235.0
	Steel(Hiten-32)	315.0

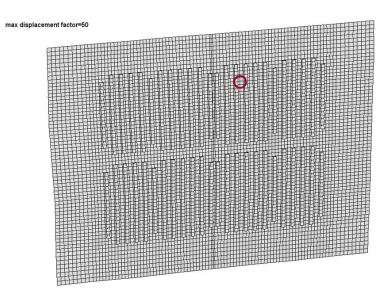

(a) failure strain 0.01 (20×20×20m)

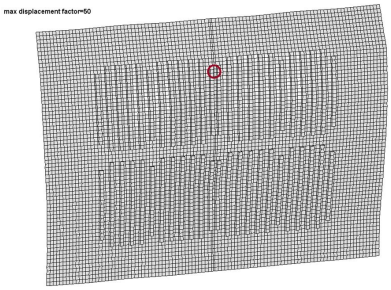

(b) failure strain 0.10 (20×20×20m)

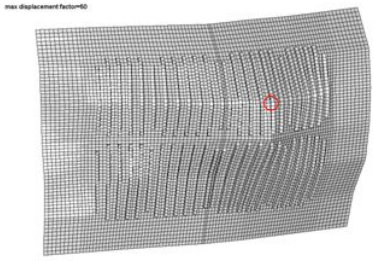

(c) failure strain 0.10 (30×30×30m)

Fig. 6.4 Local deformation configuration of segment using local zooming analysis

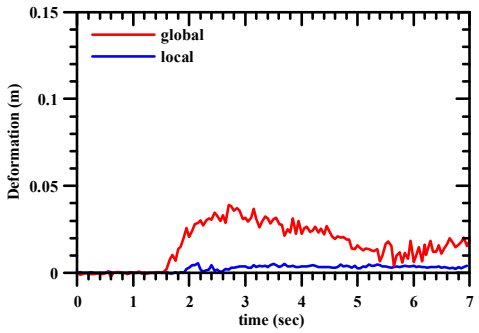

(a) failure strain 0.01 (20×20×20m)

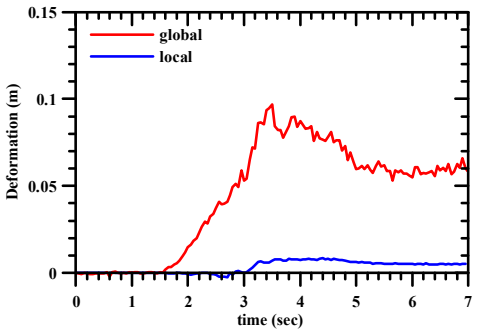

(b) failure strain 0.10 (20×20×20m)

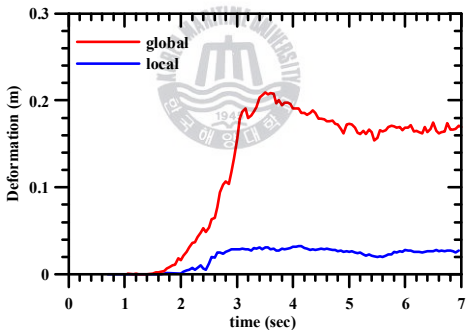

(c) failure strain 0.10 (30×30×30m)

Fig. 6.5 Response of the maximum global and local deformations in the inner hull

Figure 6.6 shows von Mises effective stress distributions of CCS components in the cases of failure strain 0.10 of 20×20×20 m cubic iceberg, where the maximum stress locations are also marked by red circle. The maximum von Mises stresses of all cases were summarized in Table 6.2 and

compared with each other case and reference ones, where reference von Mises stress was modified from component one to effective one because the every local segment in the inner hull is not oriented to the global coordinate and its local stress component can not be obtained from the Postprocessor of LS-DYNA directly.

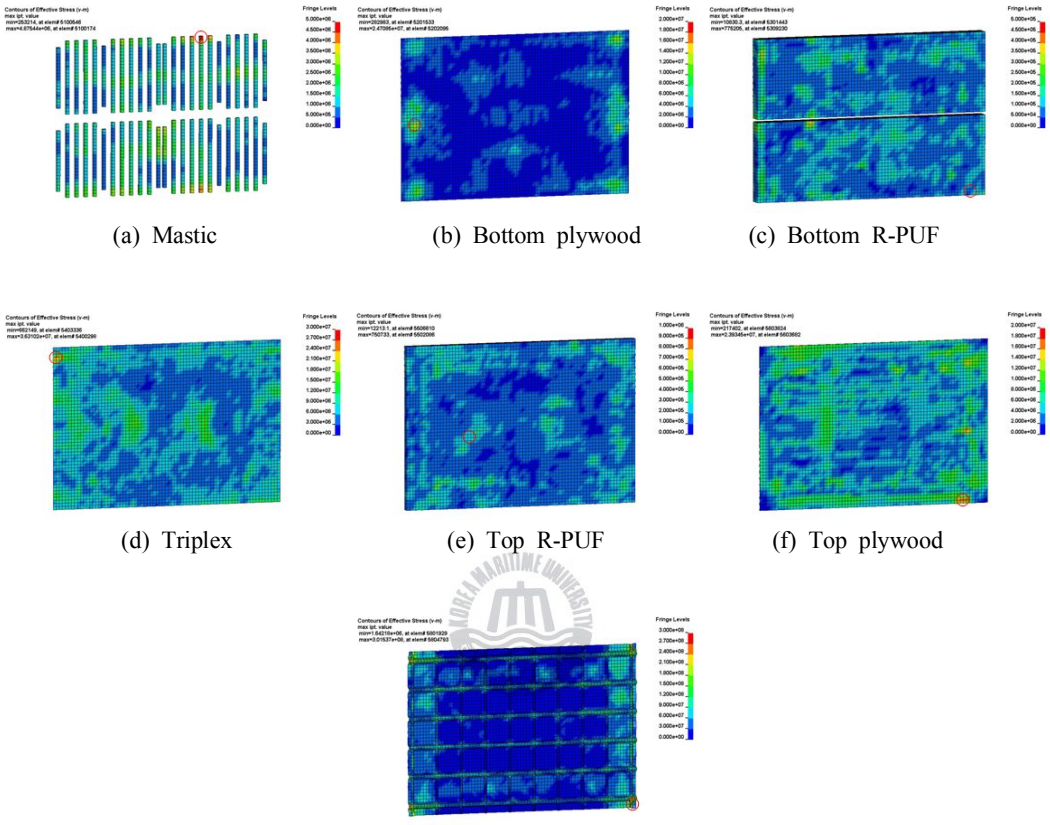

(a) Mastic (b) Bottom plywood (c) Bottom R-PUF

(d) Triplex (e) Top R-PUF (f) Top plywood

(g) Membrane

Fig. 6.6 von Mises stress distribution of each CCS component of 20×20×20m cubic iceberg with failure strain 0.10

Table 6.2 Strength evaluation of each component of CCS in each case

Material	Maximum Von Mises stress(MPa)			Reference Von Mises stress(MPa)
	0.01(20×20×20m)	0.10(20×20×20m)	0.10(30×30×30m)	
Bottom R-PUF	0.79	0.78	2.19	3.20
Top R-PUF	0.63	0.75	1.01	
Bottom plywood	19.64	24.71	64.12	34.97
Top plywood	31.90	23.93	35.69	
Triplex	23.48	36.31	33.25	
Mastic	2.71	4.88	19.23	15.00
Membrane	295.13	301.54	313.71	315.00

It could be found that the maximum von Mises stress of each component in the case of 20×20×20m cubic iceberg occurred at random place in the segment without relation to the maximum deformation, while the maximum one in the case of 30×30×30m cubic one, around the maximum deformation, which might be caused by the relative local deformation.

The allowable deformation for the safety status of NO96 membrane type CCS is 4.6 mm per unit m for operational limit, as shown in Figure 1.3, and survival limit, 40.0 mm per unit m. However, there is no information of allowable deformation limit for the MARK III membrane type CCS. Since two pieces of CCS is 3×2 meters in width and height even though its attachment method to the inner hull might be different from that of NO96 CCS, more flexible local deformation might be allowed. Maximum stress of each component has to be under the reference stress times Strength Reduction Factor (SRF, 0.8~1.0).

From the local zooming analysis results, it might be believed that the maximum local deformations, 5.6 and 8.3 mm for the cases of failure strains 0.01 and 0.10 of 20×20×20 m cubic iceberg would be within an allowable deformation criterion of MARK III membrane type CCS, and all the maximum stresses of the CCS components, also within the permissible ones except top plywood in the case of failure strain 0.01 of 20×20×20m cubic iceberg. From these results, MARK III membrane type CCS could be safe from the collision

scenario of 20×20×20m cubic iceberg of 70 degree angle of blow.

In the case of 30×30×30 m cubic iceberg, all the maximum stresses were above the permissible ones except R-PUF. Even though the maximum local deformation 32.6 mm might be allowed, its local deformation was more or less large and maximum stresses of most components were exceeded to permissible ones, such as mastic, plywood and membrane. MARK III membrane type CCS could not be safe from the collision scenario of 30×30×30m cubic iceberg of 70 degree angle of blow.

Contrary to the NO96 membrane type CCS, the crashworthiness criterion should be necessary for the impact and severe vibration forces in the case of MARK III membrane type CCS. In this chapter, the reasonable and effective procedure for the structural safety assessment technique of MARK III membrane type CCS was demonstrated under the collision scenario of iceberg using local zooming analysis from full scale iceberg-ship collision simulation.

7. Conclusions

At the time of exploitation of the giant natural gas fields in the Western Arctic regions of Russia, the development of Arctic LNG shipping has been precipitated. There have been demands for the security of design technique of Arctic LNG carrier, especially for the structural safety assessment of the Arctic LNG CCS under the impact of collision with iceberg. To develop iceberg modeling technique and to examine the characteristics of iceberg crushing strength for the more accurate and realistic full scale iceberg-membrane type LNG carrier bow shoulder collision simulations with consideration of surrounding sea water using LS-DYNA code, uniaxial compressive ice test specimen simulations in brittle and ductile failure modes were executed and diverse iceberg materials were investigated, such as its failure strain, Young's modulus, failure stress, failure tensile stress and mesh size. Local zooming analyses of MARK III membrane type LNG CCS according to iceberg sizes and failure strains were performed for the development of its structural safety assessment technique.

Among the factors concerned with iceberg materials, failure strain had an influence on the collision responses, as expected, where its crushing strength and the collision responses were increased with increase of failure strain. Failure stress, failure tensile stress and Young's modulus had a slight, a very slight and no influences on its crushing strength and the collision responses, respectively. Mesh size of ice type iceberg had a great influence on its crushing strength and the collision responses, therefore it should be considered together with its materials for the reasonable iceberg modeling.

Local zooming analysis technique has been developed using segment with the maximum deformation in the inner hull for the structural safety assessment of LNG MARK III membrane type CCS using LS-DYNA code, and it could be roughly estimated based on the operational limit and/or survival limit for

allowable deformation of NO96 membrane type CCS and the permissible stress of each component of LNG MARK III membrane type CCS. For the reasonable and reliable safety assessment of CCS, its criteria should be set up from the viewpoints of large deformation and strength of CCS under the quasi-static loading condition, and of deformation and strength of its components and its attachment to the inner hull under impact loading ones, validations should be also needed using the damage and response results of full scale iceberg-ship collision tests and iceberg material test ones at the Arctic and sub-Arctic seas.

References

[1] ABS, 2006, Guidance Notes on Strength Evaluation of Membrane-Type LNG Containment System under Sloshing Loads.

[2] Carney, Kelly S., Benson, David J., DuBois, Paul and Lee, Ryan, 2006, "A phenomenological high strain rate model with failure for ice," International Journal of Solids and Structures, Vol. 43, pp. 7820-7839.

[3] Han, S.K., Lee, J.Y., Park, Y.I. and Che, J.S., 2007, "Structural Risk Analysis of a NO96 Membrane Type LNG Carrier in the Baltic Ice Operation," 10th International Symposium on Practical Design of Ships and Other Floating Structures, Vol. II, Huston, Texas, United States of America.

[4] IOC/NRC, Bergy bit impact study.

[5] Kim, J.H., Choi, K.S. and Seo, Y.K., 2007, "Standardization of ice mechanics experimental procedures in a cold room," Journal of Ocean Engineering and Technology, Vol. 21, No. 2, pp. 60-66.

[6] Kwon, J.C., Jeon, B.Y., Kim, J.H., Wang. B., Yu, H., Basu, R., Lee, H., Daley C. and Kendrick, A., 2008, "Structural Integrity Assessment of Cargo Containment Systems in Arctic LNG Carriers under Ice Loads," Arctic Shipping 2008 Conference,Russia.

[7] Lee, S.G., Hwang, J.O. and Kim, W.S., 2008, "Wet Drop Impact Response Analysis of CCS in Membrane Type LNG Carriers I : Development of Numerical Simulation Analysis Technique through Validation," Journal of the Society of Naval Architects of Korea, Vol. 45, No. 6, pp. 726-734.

[8] Lee, S.G., Lee, J.S., Baek, Y.H. and Paik, J.K., 2009, "Development of Full Scale Iceberg-Membrane Type LNG carrier Collision Simulation Technique," Proceedings of the Annual Spring Meeting, SNAK.

[9] Lee, J.Y., Park, Y.I. and Han, S.K., 2007, "Structural Safety Assessment for Cargo Containment System of Membrane Type LNG Carrier against Ice Hazards," Proceedings of the Annual Autumn Meeting, SNAK, pp. 1330-1335.

[10] LSTC, 2007, LS-DYNA User's Manual, Version 971, Livermore Soft Technology Corp., USA.

[11] Ralston, T.D., 1977, "An Analysis of Ice Sheet Indentation," Proceedings of the IAHR Symposium on Ice Problems, Lulea, Sweden,Vol.1,pp.13-32.

[12] Sanderson, T.J.O., 1995, Ice Mechanics: Risks to Offshore Structure, Graham & Trotman.

[13] Schulson E. M., 1999, “The structural and mechanical behavior of ice,” Journal of JOM, Vol. 51, No. 2, pp. 21-27.

[14] Schulson E. M., 2001, “Brittle failure of ice,” Engineering Fracture Mechanics, Vol. 68, pp. 1839-1887.